Journal of Photochemistry and Photobiology A: Chemistry 232 (2012) 22–31

Contents lists available at SciVerse ScienceDirect

Journal of Photochemistry and Photobiology A: Chemistry

journal homepage: www.elsevier.com/locate/jphotochem

Effects of TiO_2 nanoparticle polymorphism on dye-sensitized solar cell photovoltaic properties

C. Magne[a,b], F. Dufour[c,d,e], F. Labat[a], G. Lancel[a,e], O. Durupthy[c,d,e], S. Cassaignon[c,d,e], Th. Pauporté[a,*]

[a] Chimie ParisTech, École Nationale Supérieure de Chimie de Paris, Laboratoire d'Électrochimie, Chimie des Interfaces et Modélisation pour l'Énergie, LECIME, UMR-CNRS 7575, 11 rue P. et M. Curie, 75231 Paris Cedex 05, France
[b] Saint-Gobain Recherche, 39 quai Lucien Lefranc, 93303 Aubervilliers Cedex, France
[c] UPMC Univ Paris 06, UMR 7574, Chimie de la Matière Condensée de Paris, Collège de France, 11 place Marcelin Berthelot, 75231 Paris Cedex 05, France
[d] CNRS, UMR 7574, Chimie de la Matière Condensée de Paris, Collège de France, 11 place Marcelin Berthelot, 75231 Paris Cedex 05, France
[e] Collège de France, Chaire de Matériaux Hybrides, UMR 7574, Collège de France, 11 place Marcelin Berthelot, 75231 Paris Cedex 05, France

ARTICLE INFO

Article history:
Received 18 November 2011
Received in revised form 16 January 2012
Accepted 21 January 2012
Available online 31 January 2012

Keywords:
Dye sensitized solar cell
Impedance spectroscopy
TiO_2
Polymorphism

ABSTRACT

We present a joined experimental and theoretical investigation of the TiO_2 polymorphism effects on dye-sensitized solar cells (DSSCs) photovoltaic properties. TiO_2 nanoparticles of pure anatase, pure rutile and pure brookite stabilized phases with various sizes have been prepared by solution sol–gel approaches in order to evaluate their properties in photovoltaic devices. For a valuable comparison, these various nanoparticles have been used to construct identical solar cells. Their properties have been thoroughly estimated and analysed by *J–V* curves and impedance spectroscopy measurements along with first-principles calculations based on the density functional theory (DFT) under the B3LYP approximation. In the light of DFT calculations, the open circuit voltage (V_{oc}) behavior of the solar cells is mainly explained by the dependency of the bottom of the conduction band position on the TiO_2 phase. Quantifications of electron lifetimes, transfer times, diffusion coefficients (D_{eff}) in the various polymorph TiO_2 photoanodes are also of particular importance for explaining the photovoltaic properties of the different DSSCs. We have notably found a conductivity and D_{eff} order being rutile < brookite < anatase. The comparison of anatase and brookite based-cells shows that the latter phase is very interesting for the considered application.

1. Introduction

Dye-sensitized nanocrystalline metal oxide solar cells (DSSCs) have attracted great attention in the last decade from both fundamental and applied point of views [1–7]. Due to their simple fabrication and potential low production costs they can be regarded as attractive photovoltaic devices for mass production [2,3]. TiO_2-based DSSCs can reach an overall conversion efficiency above 11% [6,7]. The wide bandgap oxide semiconductor (SC) is an important component of the cell since it acts both as the recipient of electrons injected from the photoexcited dye and as an electron transfer pathway from the dye to the front contact of the sensitized electrode [8,9]. Moreover, the oxide must be perfectly covered by a monolayer of dye in order to restrain the recombination reaction between the electrons in the oxide conduction band (CB) and triiodide in solution which limits the overall conversion efficiency of the cells. Therefore, oxide properties strongly influence the cell photovoltage, the fill factor and the quantum conversion efficiency which is determined by the light harvesting efficiency, the quantum yield of electron injection and the collection of the injected electron at the front contact. Due to this key role, the cell performances are highly dependent on the phase, the shape and the size of the oxide particles [8–10].

Three main different crystallographic phases of TiO_2, namely anatase, rutile and brookite, can be stabilized at the nanoscale [11–14]. Most of the DSSC investigations have focused on anatase particles prepared by hydrothermal synthesis [15]. Rutile has been described as giving less efficient solar cells [8,16,17]. Identical open circuit voltages (V_{oc}) have been reported by Park et al. for anatase and rutile solar cells with lower performances of rutile due to a lower dye loading and a slower electron transport [8]. However, rutile particles used in DSSCs are often significantly bigger than the anatase reference and, to our knowledge, no nanoparticles of rutile with dimensions in the 20 nm range have been compared to anatase and brookite. Up to now, interest in the brookite phase has been very scarce because it is the most difficult phase to prepare in the laboratory [18–21]. Koelsch et al. have found a rather high open circuit potential of bookite-based cells compared to the other phases [18]. Yanagida et al. [20] reported an efficiency of 4.1% with a commercial powder which was a mixture of 75% brookite and 25% anatase and not pure brookite. We can also note that DSSCs based

* Corresponding author. Tel.: +33 1 55 42 63 83.
E-mail addresses: thierry-pauporte@chimie-paristech.fr, thierry-pauporte@enscp.fr (Th. Pauporté).

1010-6030/$ – see front matter © 2012 Elsevier B.V. All rights reserved.
doi:10.1016/j.jphotochem.2012.01.015

Table 1
List of the investigated films with the morphological characteristics of the building TiO_2 particles, the bandgap and dye loading of the layers.

Film	Phase	Mean size (nm)	Particle shape	Bandgap (eV)	Dye loading without $TiCl_4$ treatment (mol L^{-1})	Dye loading with $TiCl_4$ treatment (mol L^{-1})
AREF	Anatase	17	Spheres	3.18	0.124	0.130
A3		16	Cubes	3.14	0.084	0.087
A1		9×16	Octahedrons	3.05	0.062	
A2		7×14	Octahedrons	3.01	0.027	
R1	Rutile	15×5	Rods	3.05	0.043	
R2		100×15	Rods	3.06	0.063	0.080
B1	Brookite	13	Isotropic	3.39	0.066	0.076
B2		17×10	Rice-shaped	3.36	0.064	0.073

on the monoclinic TiO_2(B) phase stabilized by phosphorous have been investigated recently, however their conversion efficiencies were low [22].

It is well-known that the DSSC performances depend on the oxide synthesis method used, on the laboratory and even on the operator. Therefore, a comparative study using data extracted from the literature is not relevant. Moreover, brookite is a very poorly documented phase for DSSC application. In the present work we have performed an extensive study of the three main TiO_2 phases (anatase, rutile and brookite) with various particle sizes for DSSC. The investigation has been carried out both at the experimental and theoretical levels. For the sake of a valuable comparison, the three phases have been produced by similar synthesis techniques performed at rather low temperature in solution. In the case of anatase, various nanoparticle sizes have been synthesized and their performances in DSSCs have been compared. Additionally, they have been compared to anatase nanoparticles obtained at higher temperature by a classical hydrothermal technique in autoclave [15]. The cell characteristics have been measured and interpreted in the light of the measured dye loading, electron lifetime and transfer time in the photoanode, layer conductivity and also with the help of periodic hybrid density functional theory calculations [23] done on selected TiO_2 polymorph slabs [24].

2. Experimental

2.1. TiO_2 nanoparticle synthesis and characterizations

The investigated TiO_2 nanoparticles with different structures are listed in Table 1. The reference anatase particles, noted AREF, were obtained from titanium isopropoxide ($Ti(OCH(CH_3)_2)_4$) precursor, according to the procedure described in detail by Ito et al. [15]. The Ti final concentration was 0.54 mol L^{-1}. The particles were prepared in an autoclave at 220 °C for 12 h. The anatase particles A1 were synthesized according to the protocol described by Dufour et al. [25]. The pH of a solution of $TiCl_4$ in 3 mol L^{-1} HCl was adjusted to 6 and the titanium load to 0.1 mol L^{-1}. Nanoparticles were synthesized by hydrothermal treatment of the suspension at 170 °C in a microwave oven for 2 h. Anatase particles A2 were synthesized according to the protocol described by Durupthy et al. [26]. A suspension was prepared by mixing $TiCl_4$ in a 3 mol L^{-1} HCl solution and glutamic acid (molar ratio 2:1). The pH was set to 4 and the Ti concentration to 0.15 mol L^{-1}. Then the solution was aged at 95 °C for 2 days. Anatase particles A3 were synthesized according to a protocol described by Sugimoto et al. [27]. A solution of Ti^{4+} was obtained by mixing a stock solution (titanium isopropoxide with triethanolamine (molar ratio 1:2)) and an oleic acid solution (molar ratio 1:5) at pH 10.5, the final concentration of Ti(IV) being 0.1 mol L^{-1}. A gel was formed by aging the solution 24 h at 100 °C. Then, the gel was transfered into an autoclave and aged at 140 °C for 3 days.

The R1 nanoparticles of rutile were synthesized by precipitation of $TiCl_3$ in deionized water. The pH of the Ti^{3+} solution was adjusted to 4 and the Ti concentration to 0.15 mol L^{-1}. The solution was then heated at 60 °C in an oven for 24 h [28]. The R2 rutile particles were obtained by refluxing a 0.15 mol L^{-1} solution of $TiCl_4$ in a 1 mol L^{-1} HCl solution for 24 h.

Two types of brookite nanoparticles, hereafter noted B1 and B2, were prepared. The brookite particles B1 were synthesized by addition of pure $TiCl_4$ in a 3 mol L^{-1} HCl solution to form a colorless solution with a Ti concentration of 0.15 mol L^{-1} [9]. The solution was heated and aged at 95 °C over 3 days and was then peptized to eliminate the rutile phase. The brookite particles B2 were obtained by co-hydrolysis of the aqueous precursors $TiCl_3$ and $TiCl_4$ with a total Ti concentration of 0.04 mol L^{-1} [29]. The pH of an equimolar solution of Ti^{3+} and Ti^{4+} was adjusted to 4.5 and the suspension was aged one week at 60 °C.

The particle shapes were determined from transmission electron images obtained with a Tecnai spirit G2 apparatus operated at 120 kV. Samples were prepared by evaporating very dilute particle suspensions onto carbon-coated grids. The obtained nanoparticles were analyzed in terms of crystalline composition with a X-ray diffractometer Brucker D8 operating in the Bragg Brentano reflection mode equipped with a nickel filter to select the Cu Kα radiation. The used references for the three structures were the JCPDS files 00-021-1272 for anatase, 00-021-1276 for rutile and 04-007-0758 for brookite.

2.2. TiO_2 film preparation and characterizations

The TiO_2 nanoparticle films were prepared according to the procedure described elsewhere [21]. A viscous paste was created by mixing the TiO_2 nanoparticles and ethylcellulose. The paste was spread onto a clean Fluoride doped tin oxide (FTO) coated glass substrates (TEC10, Pilkington) by doctor blade and sintered at 500 °C. The effect of a final $TiCl_4$ treatment consisting in immersing the TiO_2 films in a 40 mmol L^{-1} $TiCl_4$ solution at 70 °C for 30 min and annealing again at 500 °C was investigated.

The film morphologies were examined with a high resolution Ultra 55 Zeiss FEG scanning electron microscope (SEM) at an acceleration voltage of 10 kV. The film thicknesses were measured with a Dektak 6 M stylus profiler. The film structures were characterized with a X-ray diffractometer Siemens D5000 operated at 40 kV and 45 mA using the Cu Kα radiation with $\lambda = 1.5406$ Å and a rotating sample holder. The micro-Raman spectra of the films were measured using a Horiba Jobin-Yvon LabRam IR system in a backscattering configuration. The 632.8 nm line of a He–Ne laser was used for off-resonance excitation with less than 4 mW power at the sample. The optical film properties (total transmission and total reflection) were recorded with a Carry 5000 UV–vis–NIR spectrophotometer equipped with an integrating sphere.

2.3. Solar cell preparation and characterizations

The layers were sensitized by immersion upon cooling in 0.5 mmol L^{-1} N719 dye in a mixture of acetonitrile and tert-butanol (1:1) in the dark at room temperature for 24 h. The dye loading was determined by spectrophotometry, after complete dye desorption in a 0.1 mol L^{-1} KOH solution. For the counter electrode preparation, FTO glass substrates (TEC7, Pilkington) were cleaned by ultrasound in acetone and ethanol for 5 min. Then they were treated in a furnace for 30 min at 450 °C to remove organic contaminants. The Pt catalyst was deposited onto the FTO glass by coating with a drop of H_2PtCl_6 solution (6 mg Pt in 1 mL ethanol) subsequently heated at 385 °C for 30 min. The electrolyte employed was a solution of 0.6 mol L^{-1} 1,2-dimethyl-3-propylimidazolium iodide (MPII), 0.1 mol L^{-1} LiI, 0.05 mol L^{-1} I_2, 0.10 mol L^{-1} guanidinium thiocyanate and 0.5 mol L^{-1} 4-tert-butylpyridine in a mixture of acetonitrile and valeronitrile (85/15 volume ratio).

The dye-covered TiO_2 electrode and Pt-counter electrode were assembled as a sandwich type cell. A drop of the electrolyte was introduced between the electrodes by capillarity. The illuminated part of the cell corresponded to the aperture area of the black mask with a diameter of 4 mm. The device was illuminated with a solar simulator (Abet Technology Sun 2000) equipped with an AM 1.5 global air mass filter. The power density was calibrated at 100 mW cm^{-2} by using a silicon solar cell reference. The *J–V* curves were recorded by a Keithley 2400 digital sourcemeter, using a 0.01 V s^{-1} voltage sweep rate. The impedance spectra were measured at the open circuit voltage under 1 sun AM 1.5 illumination by a Solartron FRA1255 coupled with a PAR283 potentiostat. The AC signal was 10 mV and the frequency range was 100 kHz to 0.1 Hz.

2.4. DFT modeling

All calculations were carried out with the CRYSTAL code [30], which allows to self-consistently solve both the Hartree–Fock (HF) and the Kohn–Sham (KS) equations as well as to use global hybrid schemes, such as B3LYP and PBE0, using all electron Gaussian-type functions basis set through the standard LCAO approach. For oxygen and titanium, 8-411G* and 86-411G(d3) basis sets were chosen, since they have already been successfully applied to describe various properties of both bulk and surfaces of TiO_2 [23]. Throughout, the highly popular B3LYP global hybrid functional [31] was considered, since it offers a good compromise for the description of various properties of inorganic materials such as TiO_2 [32].

Modeling of surfaces was performed using slabs, that are thick slices of material (consisting of several layers) delimited by two free ideal surfaces in vacuum, obtained by bulk truncation. To provide a reliable description of an ideal surface, slabs of sufficient thicknesses have to be considered so that geometric, energetic and electronic properties are converging with respect to the number of atomic layers. Slabs of different thicknesses have thus been relaxed, and convergence has been considered using the default values of four convergence criteria based on atomic forces and displacements [30]. In addition, the irreducible Brillouin zones were sampled using $(8 \times 8 \times 8)$ and $(8 \times 8 \times 1)$ Monkhorst-Pack *k*-point mesh for the bulk and surface calculations, respectively.

3. Results and discussion

Dye-sensitized solar cells are usually fabricated using anatase nanoparticles for the porous layer preparation. TEM views of the anatase particles A1, A2, A3 and AREF are presented in Fig. 1a–d. The different average sizes were determined from XRD patterns and TEM observations. A1 particles had an elongated octahedral shape with a mean 9 × 16 nm size (Fig. 1a). A2 were elongated octahedral particles with a mean 7 × 14 nm size (Fig. 1b). A3 particles had a cubic shape with about 16 nm edge length (Fig. 1c). For the sake of comparison, spherical (truncated octahedron) anatase particles, prepared by the classical hydrothermal growth technique described by Ito et al. [15] were also imaged. Their average size was about 17 nm as shown in Fig. 1d. The dominant family of planes in octahedral anatase crystallites is the {1 0 1}. A tomographic study of the cubic anatase particles and a previous study [26] have shown the presence of {0 0 1} faces. The index of the lateral faces was unclear. The prepared rutile crystallites were elongated rods. The lateral planes of the rods are indexed to the {1 1 0} family and are the most stable. The top planes are the {1 1 1}. Two types of rutile rods were synthesized at low temperature with an average size of 15 nm × 5 nm (R1) (Fig. 1e) and 15 nm × 100 nm (R2) (Fig. 1f). Brookite was the third investigated TiO_2 phase. Particles of two different mean sizes and shapes, 13 nm for B1 with an isotropic shape and 17 nm × 10 nm for B2 with a rice-like shape, were prepared at low temperature. They are imaged in Fig. 1g and h, respectively. For brookite, the dominant surface planes of the particles were difficult to determine in part because of their aggregation. The characteristics of the various investigated particles are summarized in Table 1.

The TiO_2 nanoparticles were used to prepare porous films by doctor-blade coupled with sol–gel techniques. Fig. 2 shows that after sintering, the surface aspect of the prepared layers depended on the oxide phase. The anatase (Fig. 2a and b) and the brookite (Fig. 2d and e) films were homogeneously porous and formed of well-dispersed particles. In the case of rutile, the films were composed of rod-shaped crystallites with a tendency to aggregate (Fig. 2c). The film structures were characterized by XRD (Fig. 3 and S1) and it was checked that the initial phase was unchanged upon electrode preparation and thermal processing. Anatase has a tetragonal structure and belongs to the space group *I*4(1)/*amd* and rutile with a tetragonal structure belongs to the P4(2)/*mnm* space group. Brookite has eight formula units in the orthorhombic cell (space group *Pbca*) (Table 2). The films were also investigated by Raman spectroscopy and the spectra are presented inFig. 4 and Fig. S2 (supporting information). The anatase phase is characterized by six Raman active modes $A1_g + 2B1_g + 3E_g$ [33], and most of them are observed for A1, A2, A3 and REF films. The rutile phase has the four Raman active modes $A1_g + B1_g + B2_g + E_g$ [33] and the Raman spectra of R1 and R2 films are typical of the rutile phase. 36 Raman active modes have been described for the brookite phase [34,35]. The phase and purity of the prepared porous TiO_2 films were confirmed by the Raman measurements.

We have checked the suitability of the chosen computational protocol to model the three different polymorphs of TiO_2 which crystallographic structures are presented in Fig. S3 (supporting information). In Table 2, are gathered computed structural data for bulk anatase, rutile and brookite obtained with the method described in the experimental section. Since these materials have been extensively studied at the experimental level, well-assessed reference structural data are easily available and can be compared to the calculated parameters. Clearly, computed data are in line with available experimental ones. Errors obtained on the c lattice parameter for instance range between +0.51% for rutile, +2.70% for anatase and +0.66% for brookite. These values can be directly related to the difference of density of the three systems: anatase is almost 10% less dense than rutile ($\rho^{exp}_{rutile}/\rho^{exp}_{anatase} = 1.096$) while brookite is more similar to rutile, with only 2.5% of density difference ($\rho^{exp}_{brookite}/\rho^{exp}_{rutile} = 1.025$). The largest errors are thus computed for anatase, in which the extra volume corresponds to empty regions which would probably require to somehow take into account dispersion effects in the calculation procedure for a more accurate modeling [36]. Since we are mainly interested in a comparative

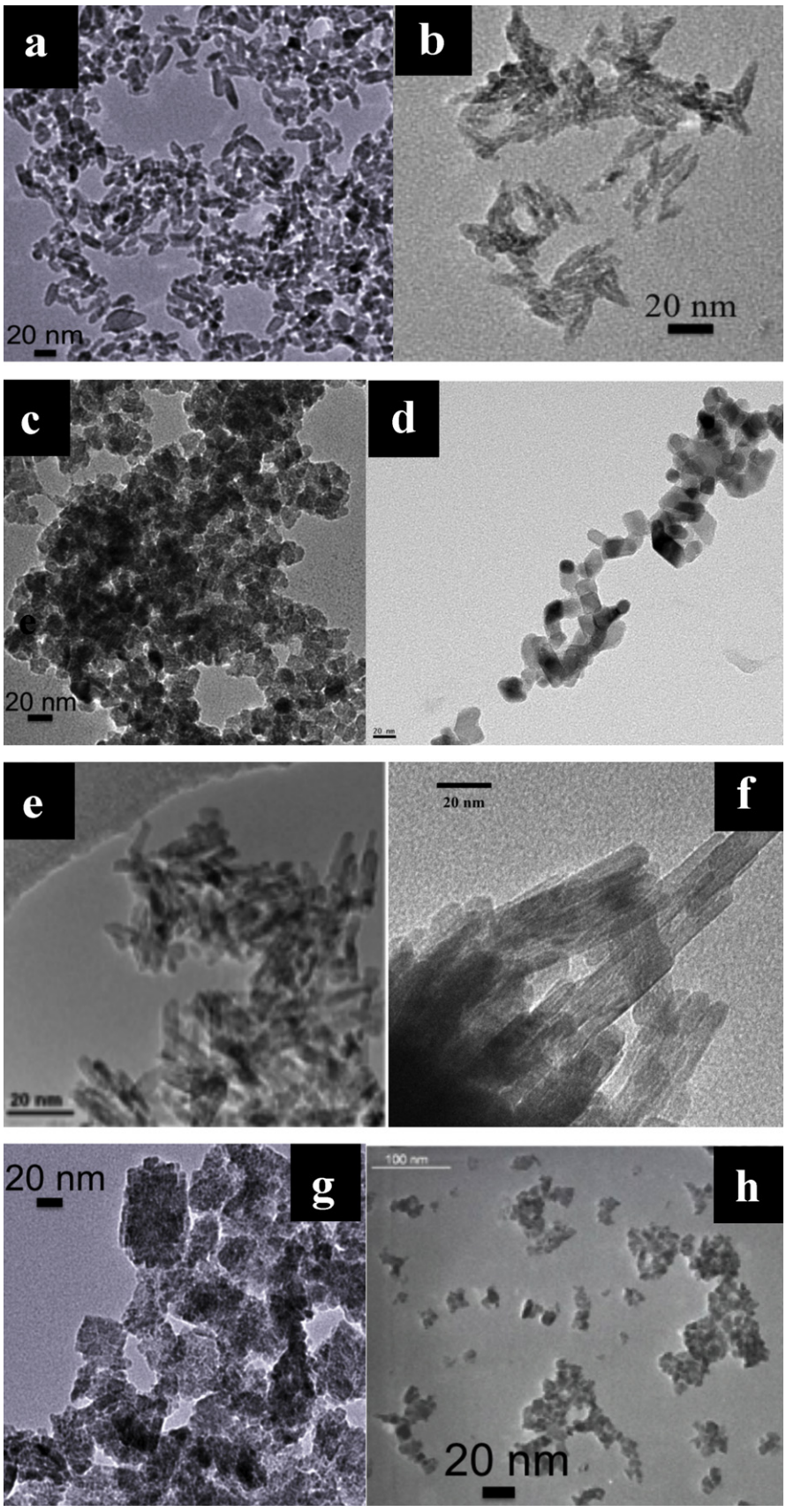

Fig. 1. TEM views and crystallite shapes of the investigated TiO_2 particles. Anatase phase: (a) A1; (b) A2; (c) A3; (d) AREF. Rutile phase: (e) R1 and (f) R2. Brookite phase: (g) B1 and (h) B2. The scale bars are 20 nm.

Table 2
Optimized crystal lattice parameters (*a*, *b*, *c* in Å), oxygen sub-lattice position (*u*, fractional units) and computed band gaps (in eV) of the three TiO_2 bulk polymorphs obtained at the B3LYP level, and comparison with experimental data.

Space group	Phase					
	Anatase *I*41/*amd* tetragonal		Rutile *P*42/*mnm* tetragonal		Brookite *Pbca* orthorhombic	
	B3LYP	JCPDS 00-021-1272	B3LYP	JCPDS 00-021-1276	B3LYP	JCPDS 04-007-0758
a	3.788	3.785	4.637	4.593	9.265	9.174
b	3.788	3.785	4.637	4.593	5.505	5.449
c	9.770	9.514	2.974	2.959	5.172	5.138
u	0.204		0.307			
Transition	Indirect		Direct		Direct	
Gap	3.97	3.15[a]	3.53	3.06[a]	4.22	3.37[a]

[a] Mean value for films prepared in this study.

study of the three investigated polymorphs, the computational protocol described above can be considered to reproduce accurately experimental trends.

The optical properties of the porous layers were characterized at the experimental level by measuring their total optical transmission and total reflectance spectra. From these data, the absorbance (A) and the absorption coefficient (α) spectra were calculated (see Fig. S4 of the supporting information) and used to determine the bandgap, noted E_g, of the various TiO_2 films. The optical bandgap, E_g, is related to the absorption coefficient according to the relationship:

$$\alpha h\nu = C(h\nu - E_g)^n \quad (1)$$

with C a constant and $n = 0.5$ for a direct transmission in the semiconductor and $n = 2$ for an indirect one. Rutile is known to be a direct semiconductor, whereas anatase is an indirect one [23]. The

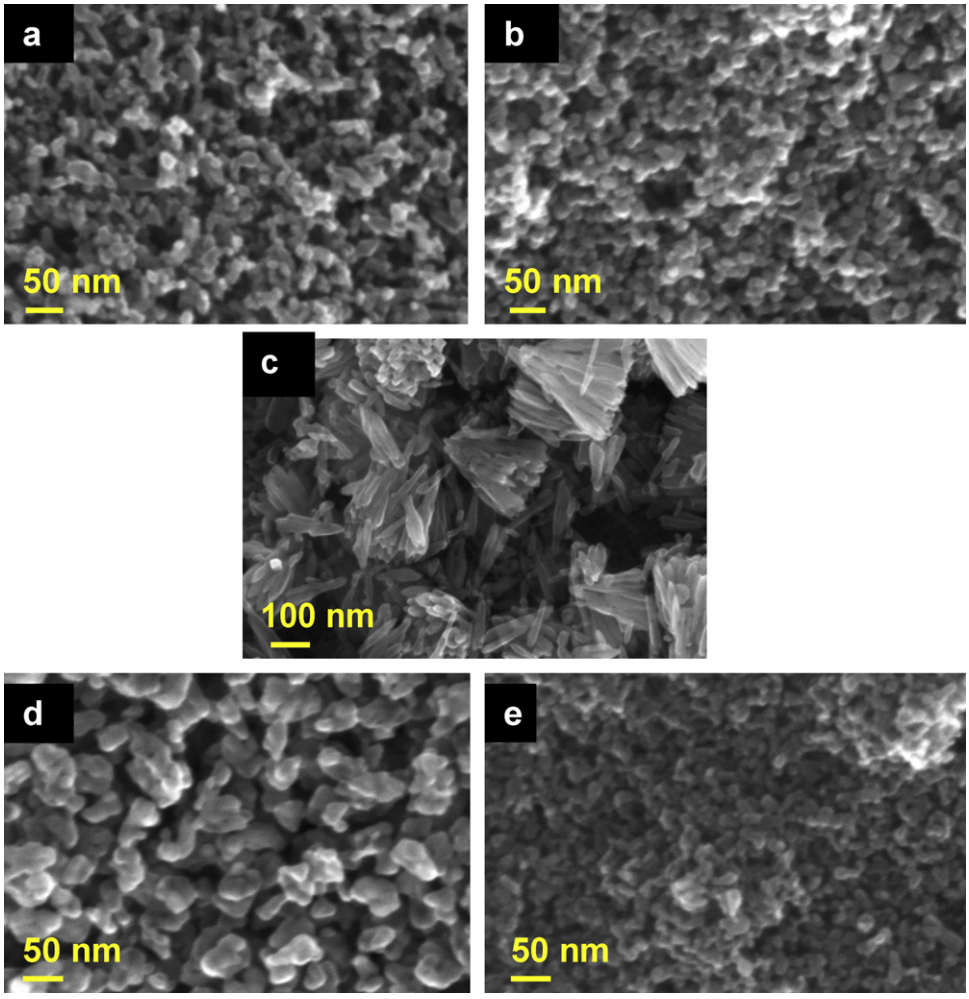

Fig. 2. SEM top views of TiO_2 films prepared with various polymorph TiO_2 particles: (a) AREF; (b) A3; (c) R2; (d) B1 and (e) B2.

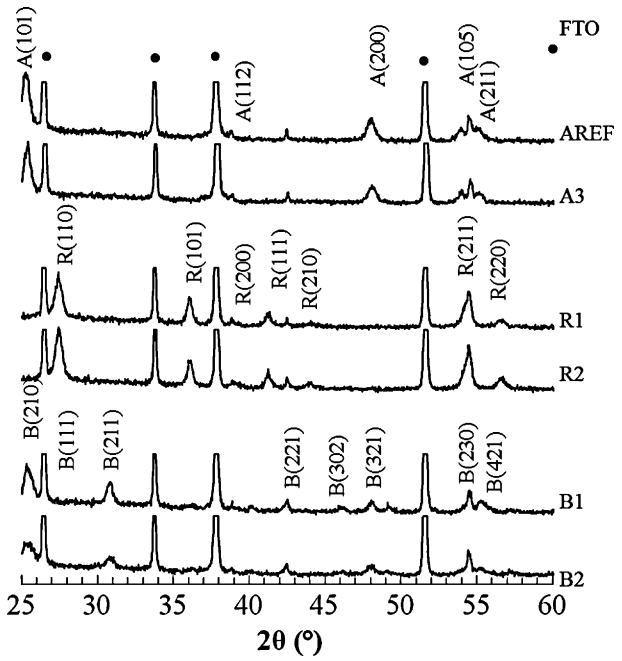

Fig. 3. XRD patterns of anatase, rutile and brookite TiO_2 nanoparticulate films. The FTO substrate reflections are marked by dark dots.

behavior of brookite is much less documented. The DFT calculations done for the present study have concluded to a direct transition at the gamma point as shown in Table 2 and Fig. S5, a result in line with previous theoretical works [37,38]. The E_g experimental values have been measured from film optical spectra and are reported in Table 1. For anatase, they ranged from 3.01 to 3.18 eV with an indirect bandgap, about 3.05 eV was found for the direct E_g of rutile and 3.36–3.39 eV for the direct E_g of brookite.

The bandgap values of the bulk TiO_2 polymorphs have been calculated. For the anatase phase, the band structure in Fig. S5 indicates that the minimum energy gap between the top of the valence band (VB) at X and the bottom of the CB at Γ is indirect with a value of 3.97 eV. For the two other phases, the band structures indicate that the minimum energy gap between the VB and the CB is direct at Γ with a value at 3.53 eV for rutile and 4.22 eV for brookite. The computed band gap energies are overestimated compared to the experimental ones but follow the same sequence rutile < anatase < brookite. The experimental trends are correctly reproduced, thus making our computational protocol suitable for a comparison of the geometric and electronic properties of these three phases.

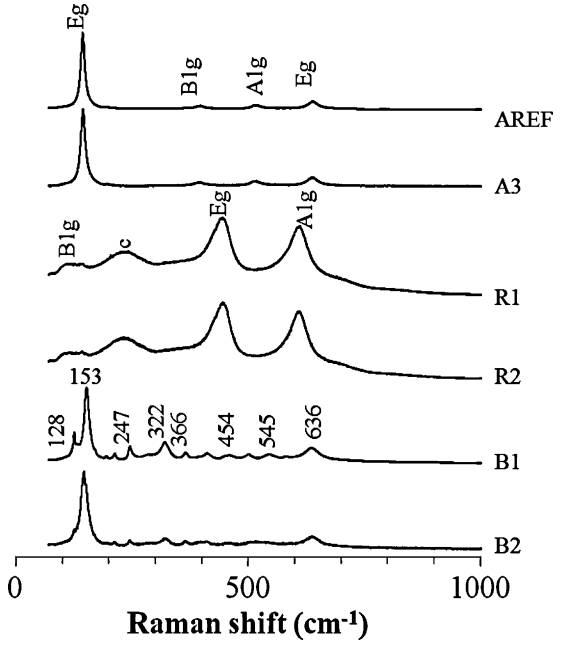

Fig. 4. Raman spectra of anatase, rutile and brookite films. The *Y*-axis is the Raman emission intensity. The strongest brookite modes are 153 cm^{-1} ($A1_g$), 247 cm^{-1} ($A1_g$), 322 cm^{-1} ($B1_g$), 366 cm^{-1} ($B2_g$) and 636 cm^{-1} ($A1_g$).

For the solar cell preparation, the porous layers were sensitized with the *cis*-diisothiocyanato-bis (2,2′-bipyridyl-4,4′-dicarboxylato) ruthenium(II) bis (tetrabutylammonium) dye (N719). Sensitization is a crucial step for DSSC fabrication because the dye acts as the sunlight absorber in the device and the dye loading of TiO_2 porous layers must be optimized to allow the maximum absorption of sunlight. This parameter was measured by desorption of N719 sensitized layers in 1 mL of concentrated KOH (pH = 13). N719 titration was done by UV–vis absorption measurements at the visible absorption maximum of the dye. The layer thicknesses (noted d) were measured precisely by profilometry and the dye loadings are reported in Table 1 as a concentration in the oxide films. The anatase hydrothermal TiO_2 nanoparticles adsorbed the largest amount of dye and Table 1 shows that this parameter decreased with anatase octahedral particle size (AREF, A1, A2). Pure brookite B1 and B2 films were less loaded than AREF anatase and had values close to A1. They adsorbed about the same dye amount despite of significant different particle shape and film morphologies as illustrated in the micrographs of Fig. 2d and e. The dye loading was also low in the case of rutile samples due to a lower amount of accessible surfaces implied by the tendency of the small rod shaped crystallites to aggregate. The dye loading was also measured after the classical $TiCl_4$ treatment of the layers. This treatment is known to give rise to an additional very thin surface layer [15]. Globally, the treatment had a beneficial impact on the dye loading and an increase of this parameter was found for the set of layers (Table 1).

Solar cells based on the various polymorphs were fabricated and their performances were evaluated by recording *J–V* curves under normalized 1 sun illumination. It is noteworthy that for a valuable comparison of the phase effects, no scattering layer was used in our work. The cell characteristics in the case of TiO_2 layers untreated by $TiCl_4$ are reported in Table 3 and the *J–V* curves are shown in Fig. S6 (supporting information). The best performances were reached for the reference hydrothermal anatase cell. Table 3 shows that for the other particles, the brookite B1 cell was the best. The rutile films yielded to the less efficient cells, notably due to rather low fill factors and low open circuit voltages compared to the brookite and anatase-based cells.

Table 4 reports the cell characteristics for the $TiCl_4$ treated TiO_2 layers and the *J–V* curves are displayed in Fig. 5 and Fig. S7 (supporting information). Results confirm the beneficial effect of this treatment on the cell performances and an improvement was observed for almost all the devices. The treatment results in an increase in J_{sc} for most anatase and brookite cells. We can also note that for rutile cells, better results of $TiCl_4$ treated cells were mainly due to higher fill factors. As regards to the V_{oc}, rutile had the lowest value, either before or after $TiCl_4$ treatment. The two other phases, anatase and brookite, without $TiCl_4$ treatment, can be compared for cells giving about the same J_{sc}, namely A1 and B1 cells. They show similar V_{oc}. We can also note that anatase particles with cubic shape give rise to a lower V_{oc} before the $TiCl_4$ treatment compared to the particles with an octahedral shape confirming the importance of the exposed surface on this solar cell parameter.

To qualitatively understand the effect of TiO_2 structure on V_{oc}, surface calculations were carried out. It is known that the maximum of the V_{oc} of a DSSC is the difference between the conduction

Table 3
Characteristics of the solar cells (short circuit current (J_{sc}), open circuit voltage (V_{oc}), fill factor (FF) and overall conversion efficiency (η)) without $TiCl_4$ treatment of the layers measured under AM1.5G, 100 mW cm^{-2} illumination.

Sample	d[a] (μm)	J_{SC} (mA cm^{-2})	V_{oc} (V)	FF (%)	η (%)
AREF	13.2	11.7	0.74	70	6.09
A1	10.7	8.7	0.71	75	4.70
A2	10.8	6.7	0.74	68	3.39
A3	12.9	9.4	0.70	75	4.94
R1	10.2	6.5	0.65	58	2.47
R2	10.3	8.2	0.66	57	3.09
B1	10.2	9.7	0.71	77	5.30
B2	14.4	7.5	0.69	78	4.02

[a] d is the porous layer thickness.

Table 4
Characteristics of the solar cells (short circuit current (J_{sc}), open circuit voltage (V_{oc}), fill factor (FF) and overall conversion efficiency (η)) with $TiCl_4$ treatment of the layers measured under AM1.5G, 100 mW cm^{-2} illumination.

Sample	d[a] (μm)	J_{SC} (mA cm^{-2})	V_{oc} (V)	FF (%)	η (%)
AREF	14.1	16.8	0.67	70	7.97
A1	11.4	8.7	0.73	75	4.71
A2	11.3	5.3	0.75	71	2.82
A3	14.4	11.0	0.70	71	5.49
R1	10.3	6.4	0.71	72	3.26
R2	11.2	8.5	0.65	63	3.53
B1	13.1	11.0	0.72	75	5.97
B2	11.6	7.4	0.76	73	4.12

[a] d is the porous layer thickness.

Table 5
Computed B3LYP surface energies (E_s) and conduction band edge energy (E_{cb}) of TiO_2 polymorphs most stable surfaces. For comparison, the LUMO energy of the N3 dye is computed at −3.18 eV (after [46]).

	Rutile (1 1 0)	Anatase (1 0 1)	Brookite (0 1 0)
Number of atoms/cell	54	30	48
E_s[a] (J m^{-2})	0.52	0.59	0.85
E_{cb} (eV)	−4.74	−4.22	−3.48

[a] Surface energies (E_s) computed as: $E_s(n) = (E_n - nE_{bulk})/2S$, where E_n is the total energy of a slab containing n Ti-layers, E_{bulk} is the bulk energy of the infinite system per unit cell (taken from an independent bulk calculation), and S is the area of the slab. The (1/2) factor takes into account the existence of two free surfaces for each slab.

band energy level in the semiconductor and the redox couple energy level in the electrolyte [39]. In Table 5, we report the computed energies of the bottom of the conduction band (CB) for the most stable low-index planes of the three TiO_2 polymorphs under investigation. The (1 0 1) plane of anatase has been modeled because the {1 0 1} family of planes is dominant in octahedral anatase crystallites. The (1 1 0) plane of rutile was chosen because the {1 1 0} family of plane is the most present in rod shaped rutile nanoparticles. In the case of brookite, no dominant low-index planes were clearly found for our particles. Following a previous DFT work [38], the (0 1 0) plane was chosen as it was shown to be the most stable. Although some high energy surface orientations in gas-phase such as anatase (0 0 1) have recently been shown to become preferentially exposed when an implicit solvation model is considered at the theoretical level [40,41], no solvation effects could be included in our periodic calculations, as the present version of the CRYSTAL code does not implement such a model. We therefore only considered the main orientations found in the TEM observations of our particles, when possible.

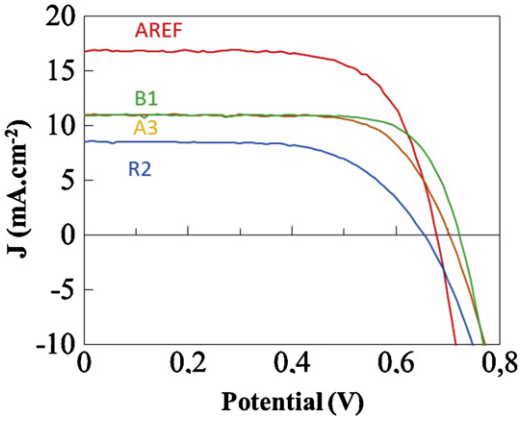

Fig. 5. J–V curves of the $TiCl_4$ treated AREF, A3, R2 and B1 solar cells under AM1.5G, 100 mW cm^{-2} illumination.

We note that only clean surfaces in the gas-phase have been taken into account, without considering adsorption of the above mentioned dye or additives present in the electrolyte [42]. We can however reasonably expect that the dye and additives binding to the different surfaces occurs through similar modes in all cases, thus shifting the clean surfaces CB energy similarly upon dye/additive adsorption. From the computed surface data reported in Table 5: E_{cb} (rutile) < E_{cb} (anatase) < E_{cb} (brookite), suggesting a V_{oc} increase when going from rutile to anatase and brookite. The theoretical study is in line with experimental results in the case of rutile compared to the other two phases. The experimental data give similar V_{oc} for anatase and brookite. The computed surface energies of the considered crystallographic planes of the polymorphs are also reported in Table 5 and show the following stability order: rutile (1 1 0) < anatase (1 0 1) < brookite (0 1 0). Although this order might be modified in solution, due to preferential

Table 6
Recombination and electronic transfer properties of the polymorph TiO_2 films determined by fitting EIS spectra measured at the V_{oc} under AM1.5G, 100 mW cm^{-2} illumination.

Sample	$TiCl_4$	ω_{rec} (s^{-1})	ω_d (s^{-1})	Lifetime τ_{rec} (ms)	Transfer time τ_d (ms)	τ_{rec}/τ_d	σ (mS cm^{-1})	D_{eff} ($\times 10^{-5}$ cm^2 s^{-1})	L_d (μm)
AREF		37	161	170	39	4.3	3.4	4.45	27
	X	21	122	300	52	5.8	7.2	3.79	34
A1		21	60	300	105	2.9	1.7	1.09	18
	X	19	65	336	96	3.5	1.8	1.35	21
A2	X	40	70	159	90	1.8	1.6	1.42	15
A3		30	101	213	62	3.4	2.6	2.67	24
	X	21	70	298	89	3.3	2.7	2.33	26
R1		9	21	671	303	2.2	0.5	0.34	15
	X	11	23	554	271	2.0	0.3	0.39	15
R2		10	30	651	212	3.1	0.9	0.50	18
	X	10	47	628	132	4.7	1.3	0.95	24
B1		13	31	490	203	2.4	1.7	0.55	16
	X	15	58	430	108	4.0	2.6	1.05	26

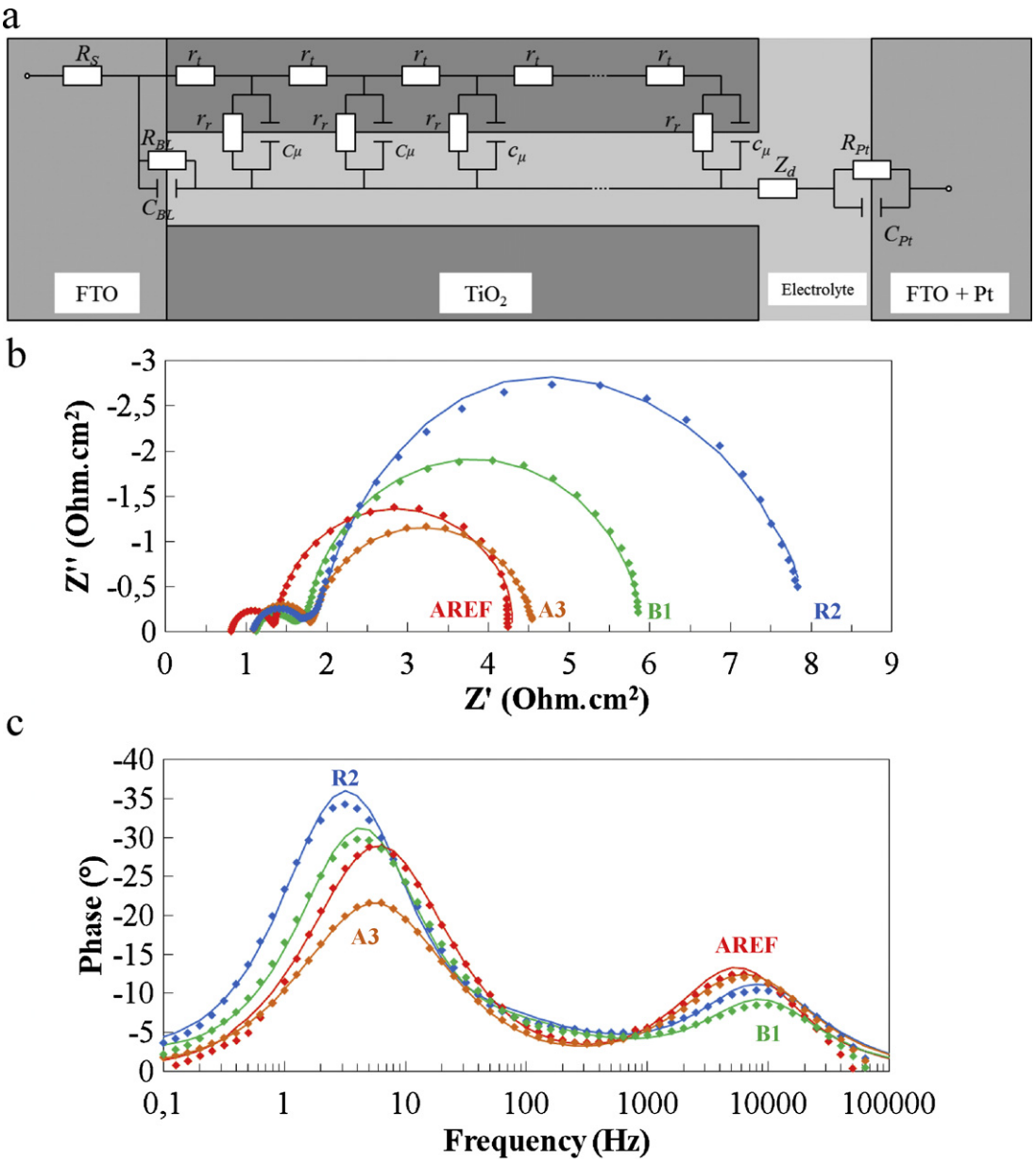

Fig. 6. Impedance spectra of the best $TiCl_4$ treated solar cells recorded at the V_{oc} under 100 mW cm^{-2}, AM1.5G. (a) Equivalent circuit used to fit the spectra, (b) Nyquist plot and (c) phase versus frequency plot of the AREF, A3, R2 and B1 solar cells. The dots are the experimental values and the full lines are the best fits.

stabilization of some orientations by solvent molecule dissociation (see Refs. [40,41] for instance), data reported for the three considered polymorphs are in nice agreement with the previously reported gas-phase data [23,38].

To better understand the TiO_2 phase effects on DSSC operation, electrochemical impedance spectroscopy (EIS) measurements were conducted at the open circuit voltage under 1 sun illumination [43–45]. The spectra are displayed in Figs. S8–S9 (supporting information) and Fig. 6 for untreated and $TiCl_4$ treated TiO_2 layers, respectively. They are characterized by two arc-of-a-circles: the high frequency relaxation is classically assigned to the redox reaction at the charged counter electrode and the low frequency relaxation is due to the injection/recombination reactions and electron diffusion in the photoanode. The equivalent electrical circuit used to fit the EIS spectra is shown in Fig. 6a [2]. The low frequency part of the spectra is characterized by two relaxation constants noted ω_{rec} and ω_d. The former is characteristic of the electron lifetime and recombination in the photoanode, with $\tau_{rec} = 2\pi/\omega_{rec}$, and the latter is typical of the electron transfer time, with $\tau_d = 2\pi/\omega_d$. The equivalent circuit parameters, determined from the spectrum fits, are reported in Table S1 of the supporting information. The spectra were fully analysed to determine τ_{rec} and τ_d and the data are reported in Table 6. For a correct photoanode functioning, the latter must be much shorter than the former. In most case τ_d was reduced by the $TiCl_4$ treatment and better τ_d/τ_{rec} ratio were found for the treated cells. As expected, the cells with the best power conversion efficiency were those with the highest τ_d/τ_{rec} ratio, namely AREF, A3, R2 and B1. In Table 6, we can note that the lifetimes and the transfer times are longer in the case of the brookite and the rutile phases compared to the anatase phase.

The conductivities of the oxide films constituting the photoanodes were calculated according to the following equation:

$$\sigma = \frac{d}{S(1-p)R_t} \quad (2)$$

where d is the layer thickness, R_t is the transfer resistance, p is the film porosity (60%) and S is the projected area of the photoanode. The corresponding results are reported in Table 6. The best conducting phase is the AREF anatase ($7.2\ mS\ cm^{-1}$) which has the shortest transfer time and gives rise to the best solar cells. If we consider the set of anatase-based photoanodes, the conductivity decreases with decreasing anatase particle size. It can be explained by an increasing number of interparticle boundaries at constant layer thickness that hinder the electronic transfer between the dye and the front contact. In Table 6, we can see that, in most cases, the conductivity of the various phases increases with the $TiCl_4$ treatment. We can conclude that the beneficial effect of the treatment is twofold: (i) it improves the dye loading and (ii) it gives rise to higher layer conductivities.

The diffusion coefficient of the electrons in the photoanode, noted D_{eff}, was also calculated from the EIS measurements and fits. D_{eff} is determined by using the τ_d value in the following equation:

$$D_{eff} = \frac{d^2}{\tau_d} \quad (3)$$

The calculated values are reported in Table 6. We observe an increasing D_{eff} with increasing anatase particle size. The A1, A2, R1 and R2 photoanodes have rather low D_{eff} which explain, in part, their poor photovoltaic performances. In Table 6, we have also reported the average distance that electron diffuses before undergoing electron transfer to the redox species, the electron diffusion length noted L_d. In the case of first order recombination kinetics, L_d equals to $(D_{eff}\tau_{rec})^{1/2}$. For efficient collection of electrons at the anode, L_d needs to be more than 2–3 times greater than the film thickness. As expected, the best cells have the highest L_d.

Globally, for σ and for D_{eff} the TiO_2 polymorphs are clearly ordered as rutile < brookite < anatase. However, large variations are observed depending on the size and the synthesis conditions of the starting building blocks. This point is for instance well-illustrated by the anatase films. Indeed, films composed of bigger nanoparticles display better electron diffusion coefficients.

If we compare the best untreated cells for the three investigated phases, namely AREF, A3, R2 and B1 (especially A3, R2 and B1 which have similar dye density), we can observe that rutile has the lowest efficiency with lower values of J_{sc}, V_{oc} and FF. Anatase and brookite have similar solar cell parameters. The conductivity of brookite is measured lower than that of anatase but it has longer electron lifetime. Similarly, for the $TiCl_4$ treated cells, it is of interest to compare A3, R2 and B1 which have about the same dye density. The J_{sc} and FF of R2 are increased by the treatment but remain lower than for the two other phases. We can suppose that the injection efficiency is not very high in rutile in spite of the low computed conduction band edge energy of this phase (Table 5). An interesting result of the present study is the good performances of the brookite phase, which has been poorly investigated up to now for DSSC application [20,29]. This is illustrated by the comparison of A3 and B1 cells, which have a similar dye loading. B1 has a slightly higher value of η because of a better $V_{oc.}$ This shows that the brookite phase has promising unexplored properties for DSSC applications and further investigations should be devoted to the increase in brookite film dye loading and conductivity.

In summary, we have made a comparative study of a set of TiO_2 nanoparticles prepared by similar growth techniques in solution for DSSC application. The effect of the three main crystallographic phases that can be stabilized at the nanoscale, namely pure anatase, rutile and brookite, with various sizes has been thoroughly investigated. The resulting nanoparticle porous films have been characterized from the structural and optical point of views prior to be used for DSSC preparation and characterizations. The cell performances were improved after a $TiCl_4$ treatment due to a higher dye loading and oxide film conductivity. We show that the open circuit voltage (V_{oc}) of the cells ranges in the following order rutile < anatase and brookite. First-principles calculations based on the density functional theory under the B3LYP approximation have help us to explain this behavior by the fact that the bottom of the CB position depends on the TiO_2 phase. The set of investigated anatase particles shows better results for particles hydrothermally grown at rather high temperature and a decrease in the cell performances with decreasing the particle size. The cell operation under illumination has been thoroughly investigated by impedance spectroscopy (IS). The electron lifetime, transfer time in the photoanode, electron diffusion coefficient and layer conductivies have been determined. We have notably found a conductivity and D_{eff} order being rutile < brookite < anatase. The results reported for the much less studied brookite phase are interesting and further investigations are ongoing to increase the film dye loading and conductivity.

Acknowledgements

Contance Magne and Dr. Thierry Pauporté acknowledge Saint Gobain Recherche (Aubervilliers, France) for its support. Dr. O. Lupan (ENSCP (France) and Technical University of Moldova (Republic of Moldova)) is acknowledged for Raman spectrum measurements. This work received the financial support from the C-nanoîle-de-France programme (hybrid-PV project).

Appendix A. Supplementary data

Supplementary data associated with this article can be found, in the online version, at doi:10.1016/j.jphotochem.2012.01.015.

References

[1] B. O'Regan, M. Grätzel, Nature 353 (1991) 737.
[2] K. Kalyanasundaram ed., Dye-sensitized Solar Cells, EPFL Press, Lausanne, 2010.
[3] A. Hagfeldt, G. Boschloo, L. Sun, L. Kloo, H. Pettersson, Chem. Rev. 110 (2010) 6595.
[4] G. Smestad, Sol. Energy Mater. Sol. Cell 32 (1994) 259.
[5] L. Han, A. Fukui, Y. Chiba, A. Islam, R. Komiya, N. Fuke, N. Koide, R. Yamanaka, M. Shimizu, Appl. Phys. Lett. 94 (2009) 013305.
[6] Q. Yu, Y. Wang, Z. Yi, N. Zu, J. Zhang, M. Zhang, P. Wang, ACS Nano 4 (2010) 6032.
[7] A. Yella, H.W. Lee, H.N. Tsao, C. Yi, A.K. Chandiran, M.K. Nazeeruddin, E.W. Diau, C.-Y. Yeh, S.M. Zakeeruddin, M. Grätzel, Science 334 (2011) 629–634.
[8] N.G. Park, J. Van de Lagemaat, A.J. Franck, J. Phys. Chem. B 104 (2000) 8989.
[9] O. Lupan, V.M. Guérin, I.M. Tiginyanu, V.V. Ursaki, L. Chow, H. Heinrich, T. Pauporté, J. Photochem. Photobiol. A 211 (2010) 65.
[10] V.M. Guérin, C. Magne, T. Pauporté, T. Le Bahers, J. Rathousky, ACS Appl. Mater. Interface 2 (2010) 3677.
[11] A. Pottier, C. Chanéac, E. Tronc, L. Mazerolles, J.P. Jolivet, J. Mater. Chem. 11 (2001) 1116.
[12] M. Koelsch, S. Cassaignon, J.F. Guillemoles, J.P. Jolivet, Thin Solid Films 403–404 (2002) 312.
[13] A. Pottier, S. Cassaignon, C. Chaneac, F. Villain, E. Tronc, J.P. Jolivet, J. Mater. Chem. 13 (2003) 877.
[14] S. Cassaignon, M. Koelsch, J.P. Jolivet, J. Phys. Chem. Solids 68 (2007) 695.
[15] S. Ito, T.N. Murakami, P. Comte, P. Liska, C. Grätzel, M.K. Nazeeruddin, M. Grätzel, Thin Solid Films 516 (2008) 4613.
[16] W. Yang, F. Wan, Y. Wang, C. Jiang, Appl. Phys. Lett. 95 (2009) 133121.
[17] H.Y. Byun, R. Vittal, D.Y. Kim, K.J. Kim, Langmuir 20 (2004) 6853.
[18] M. Koelsch, S. Cassaignon, T.T. Minh, J.F. Guillemoles, J.P. Jolivet, Thin Solid Films 451–452 (2004) 86.
[19] E. Lancelle-Beltran, P. Prene, C. Boscher, P. Belleville, P. Buvat, S. Lambert, F. Guillet, C. Marcel, C. Sanchez, Eur. J. Inorg. Chem. 6 (2008) 903.
[20] K.J. Jiang, T. Kitamura, H. Yin, S. Ito, S. Yanagida, Chem. Lett. 9 (2002) 872.
[21] C. Magne, S. Cassaignon, G. Lancel, T. Pauporté, ChemPhysChem 12 (2011) 2461.
[22] J. Procázka, L. Kavan, M. Zukalavá, O. Franck, M. Kalbác, A. Zukal, M. Klementová, D. Carbone, M. Grätzel, Chem. Mater. 21 (2009) 1457.
[23] F. Labat, P. Baranek, C. Domain, C. Minot, C. Adamo, J. Chem. Phys. 126 (2007) 154703.
[24] F. Labat, P. Baranek, C. Adamo, J. Chem. Theory Comput. 4 (2008) 341.
[25] F. Dufour, S. Cassaignon, O. Durupthy, C. Colbeau-Justin, C. Chanéac, Eur. J. Inorg. Chem. (2011), doi:10.1002/ejic.201101269.
[26] O. Durupthy, J. Bill, F. Aldinger, Cryst. Growth Des. 7 (2007) 2696.
[27] T. Sugimoto, X. Zhou, A. Muramatsu, J. Colloid Interface Sci. 259 (2003) 53.
[28] S. Cassaignon, M. Koelsch, J.P. Jolivet, J. Phys. Chem. Solids 68 (2007) 695–700.
[29] C. Perego, I. Clemençon, B. Rebours, R. Revel, O. Durupthy, S. Cassaignon, J.P. Jolivet, Mater. Res. Soc. Symp. Proc. (2009) 1146E.
[30] V.R. Saunders, R. Dovesi, C. Roetti, R. Orlando, C.M. Zicovich-Wilson, N.M. Harrison, K. Doll, B. Civalleri, I. Bush, P. D'Arco, M. Llunell, Crystal 09. User's Manual, Università di Torino, Torino, Italy, 2009.
[31] P.J. Stephens, F.J. Devlin, C.F. Chabalowski, M.J. Frisch, J. Phys. Chem. 98 (1994) 11623.
[32] Y.F. Zhang, W. Lin, Y. Li, K.N. Ding, J.Q. Li, J. Phys. Chem. B 109 (2005) 19270.
[33] A. Chaves, K.S. Katiyan, S.P.S. Porto, Phys. Rev. 10 (1974) 3522.
[34] G.A. Tompsett, G.A. Bowmaker, R.P. Cooney, J.B. Metson, K.A. Rodgers, J.M. Seakins, J. Raman Spectrosc. 26 (1995) 57.
[35] T. Ohsaka, F. Izumi, Y. Fujiki, J. Raman Spectrosc. 7 (1978) 321.
[36] J.C. Conesa, J. Phys. Chem. C 114 (2010) 22718.
[37] S.D Mo, W.Y. Ching, Phys. Rev. B 55 (1995) 13023.
[38] A. Beltrán, L. Gracia, J. Andrés, J. Phys. Chem. B 110 (2006) 23417.
[39] T. Le Bahers, F. Labat, T. Pauporté, I. Ciofini, Phys. Chem. Chem. Phys. 12 (2010) 14710.
[40] Y.-F. Li, Z.-P. Liu, L. Liu, W. Gao, J. Am. Chem. Soc. 132 (2010) 13008.
[41] Y.-F. Li, Z.-P. Liu, J. Am. Chem. Soc. 133 (2011) 15743.
[42] T. Le Bahers, F. Labat, T. Pauporté, P. Lainé, I. Ciofini, J. Am. Chem. Soc. 133 (2011) 8005.
[43] J. Bisquert, J. Phys. Chem. B 106 (2002) 325.
[44] J. Bisquert, V.S. Vikhrenko, J. Phys. Chem. B 108 (2004) 2313.
[45] Q. Wang, J.E. Moser, M. Grätzel, J. Phys. Chem. B 109 (2005) 14945.
[46] F. Labat, I. Ciofini, C. Adamo, J. Phys. Chem. C 115 (2011) 4297.